

Two-level System Loss: Significant not only at Millikelvin

W. Shan and S. Ezaki

National Astronomical Observatory of Japan, Mitaka, Tokyo, 181-8588, Japan

(Dated: 12 July 2024)

Two-level system (TLS) loss in amorphous dielectric materials has been intensively studied at millikelvin temperatures due to its impact on superconducting qubit devices and incoherent detectors. However, the significance of TLS loss in superconducting transmission lines at liquid helium temperatures remains unclear. This study investigates TLS loss in amorphous SiO₂ at liquid helium temperatures (about 4 K) within a frequency range of 130-170 GHz, using niobium microstrip and coplanar waveguide resonators. Our results demonstrate notable power and temperature dependence of dielectric loss, with the dielectric loss and quasiparticle loss exchanging dominance at around 4 K. These findings are consistent with TLS models and provide crucial insights for the design of superconducting devices operating at liquid helium temperatures.

The superconducting state significantly reduces conducting loss, making other types of loss more prominent. Among these, extrinsic dielectric loss due to two-level systems (TLSs) has been extensively studied at millikelvin temperatures (1-400 mK), primarily driven by advancements in superconducting quantum devices and kinetic inductance detectors (KIDs) based on superconducting microwave resonators. This is because TLS loss plays a critical role in determining the coherent time of qubits and the sensitivity of the detectors¹. In contrast, at liquid helium temperature (approximately 4 K), there has been surprisingly little experimental assessment of dielectric loss. This is despite the fact that various superconducting electronic devices operate at this temperature, including Josephson voltage standards², rapid single flux quantum logic^{3,4}, hot electron bolometers^{5,6}, and superconductor-insulator-superconductor (SIS) heterodyne mixers covering wide frequency range from millimeter wave to terahertz frequencies⁷⁻¹¹. Even at intermedium sub-kelvin temperatures (0.4-1 K), the TLS loss of amorphous dielectric material has not been fully assessed, although it may be relevant for certain applications, such as antenna-coupled transition edge sensors (TES)^{12,13}.

A conventional niobium SIS mixer circuit uses amorphous SiO₂ as the dielectric layer for superconducting microstrip (MS) lines in tuning circuits and impedance transformers. SiO₂ is chosen for these circuits due to its low permittivity ($\epsilon_r \approx 4$), in addition to superior chemical and mechanical stability. A low permittivity allows for a higher achievable characteristic impedance in microstrip lines, given the minimum strip width allowed in fabrication. This flexibility in selecting characteristic impedance is crucial for designing broadband tuning circuits and impedance matching networks between the low-impedance SIS junctions and the higher-impedance waveguides.

Conventionally designed SIS mixers usually contained electrically short transmission lines, typically less than one wavelength. As a result, dielectric loss was unlikely to cause noticeable degradation in the performance and thus received little attention. This is similar to the tolerance of quasiparticle loss at 4 K operation. However, advancements in SIS mixer technology have led to the use of larger-scale on-chip systems for compactness¹⁴⁻¹⁶, multibeam^{17,18}, and multi-band¹⁹, which involve significantly longer transmission lines. In these

applications the accumulation of the losses from the dielectric layer may become pertinent.

There might be a mistaken belief that the TLS loss is negligible at 4 K due to the convergence of the occupations of the two states. However, thermalization depends on energy splitting, which has a broad distribution^{20,21}. While TLS loss is not expected to be significant at microwave around 4 K, it can become important at millimeter and sub-millimeter wave lengths. Indeed, if frequency and temperature increase by the same factor, the TLS loss does not change because it depends on the normalized temperature with respect to $\hbar\omega/k_B$, appearing as a factor in the standard TLS loss model:

$$\delta(T, \omega, P) = F \delta_{TLS}^0(\omega) \frac{\tanh \frac{\hbar\omega}{2k_B T}}{\sqrt{1 + \frac{P}{P_c}}}, \quad (1)$$

where δ_{TLS}^0 is TLS loss at 0 K and low power ($P \ll P_c$), P_c is saturation power, and ω , T , k_B are angular frequency, temperature, and Boltzmann constant respectively. F is the filling factor of the lossy dielectric material, which is close to 1 for an MS. δ_{TLS}^0 , reflecting the density of state of TLSs, is smoothly dependent on frequency on the scale of $k_B T$ ²⁰. This equation suggests that TLS loss at 160 GHz and a temperature of 4 K will be comparable to that at 4 GHz and 100 mK.

Loss measurements of superconducting thin-film transmission lines at millimeter wave frequencies and 4 K have primarily relied on on-chip SIS detectors^{22,23}. This approach is favored because constructing a planar circuit-to-metal waveguide transition, which is necessary for network analyzer measurements, is challenging. However, the low saturation power (microwatt level) of SIS detectors limits the ability to identify the TLS nature from the power-dependence property, as these detectors saturate well below P_c . Although high-dynamic range measurements using network analyzers become less challenging at microwave frequencies, due to the use of coaxial cables to access planar circuits, TLS loss is heavily suppressed due to thermalization at 4 K. This suppression makes it difficult to distinguish TLS loss from the more significant quasiparticle loss. Notably, a network analyzer-based measurement of SiO₂ loss was conducted at 70-75 GHz and 4.2 K using a fin-line microstrip-to-waveguide transition²⁴. However, this study did not address the nature of the dielectric loss.

We measured SiO₂ loss from the Q factor of half-

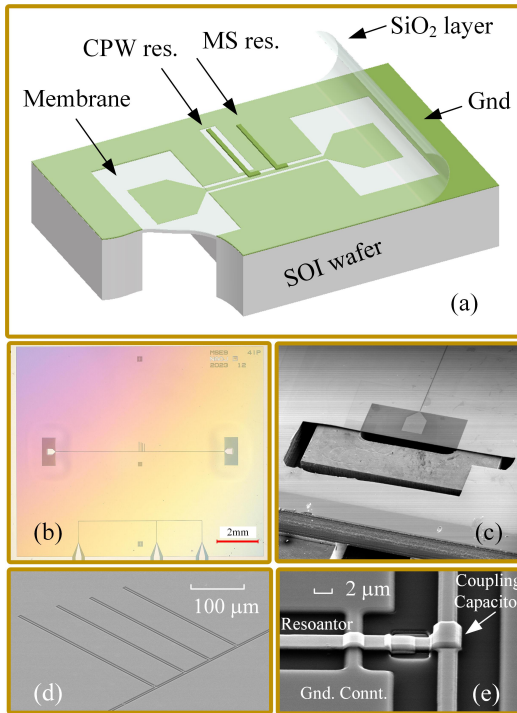


FIG. 1. (a) Schematic illustration of the on-chip two-port measurement network interfaced by a pair of silicon membrane-based waveguide-to-CPW transitions. A CPW resonator and an MS resonator capacitively couple to the readout CPW, which connects the two probes. An amorphous SiO_2 dielectric layer is sandwiched between the conducting strips of the resonators and the ground plane. The mounting structure for the chip is detailed in the appendix. (b) photo of a chip. (c) SEM image of the silicon membrane which was broken for demonstration purpose. (d) SEM image of four CPW resonators. (e) SEM image of a coupling T-junction that couples a CPW resonator to the readout line. The ground planes on both sides of the CPW resonator are connected near the T-junction to avoid generating differential mode at the discontinuity.

wavelength niobium MS and coplanar waveguide (CPW) resonators, resonating in the frequency range between 130 - 170 GHz, and being fabricated on silicon chips. Each chip contains four resonators, spaced approximately 10 GHz apart, and coupled in parallel to a readout CPW, as shown in Fig. 1. The niobium films, deposited using DC magnetron sputtering, have a thickness of about 200 nm, sufficiently thicker than the penetration depth at 4 K. These films exhibit a T_c of about 9 K and a residual resistivity of about $4.2 \mu\Omega\text{cm}$. The amorphous SiO_2 dielectric layer for the MS was deposited using plasma enhanced chemical vapor deposition (PECVD) or magnetron RF sputtering. Since the SiO_2 layer covers the entire wafer above the niobium ground plane, it also lies between the strip and ground plane of the CPW resonators, resulting a filling factor $F \approx 0.17$. The details of resonator designs can be found in the appendix. The chips containing resonators were cooled down in a cryostat by using a close-cycled GM cooler to a minimum stage temperature approximately 3.3 K, monitored with a calibrated temperature sensor. The stage can be heated up to the transition temperature of the niobium using a

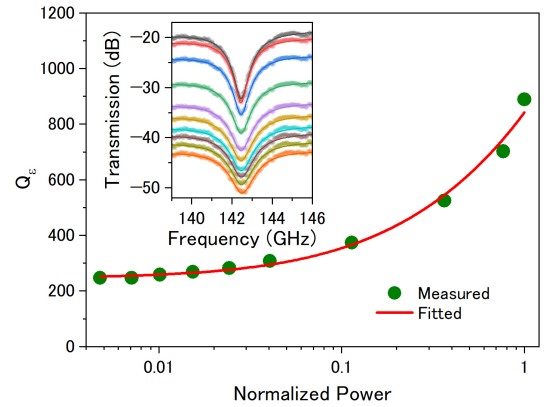


FIG. 2. Dielectric Q factor (Q_ϵ) of an MS resonator measured at 3.3 K against signal power (dots), which is normalized to approximately $3 \mu\text{W}$ at zero attenuation. The SiO_2 layer of this sample was deposited using PECVD. The inset shows the measured and fitted resonance curves of the resonator at various power levels.

heater.

The measurement was carried out with a millimeter wave network analyzer. The silicon membrane-based waveguide-to-CPW transition embedded in the silicon wafer enable the transition from the CPW to the external WR-6 waveguide for connecting the network analyzer. Despite of a high permittivity of silicon, due to the very short electric length inside the $6\text{-}\mu\text{m}$ thick membrane, the frequency-dependence in the transmission characteristics can be well suppressed. In consequence, this waveguide-to-CPW transition has a high coupling efficiency with a return loss less than -15 dB over a broad bandwidth covering 125 - 211 GHz²⁵. A pair of such transitions are deployed back-to-back on the silicon chip, constructing a versatile and general-purpose test platform for the assessment of two-port planar circuit components. Details of the measurement setup can be found in the appendix.

Calibrating the network analyzer at cryogenic temperatures is usually more demanding than at room temperature. However, cryogenic calibration can be avoided here for two reasons. First, only the amplitude of transmission response is needed. Second, the amplitude of standing waves caused by discontinuities in the measurement path external to the network analyzer was carefully minimized, achieving a low ripple less than 0.25 dB in RMS within the 130-170 GHz band. Since standing waves of this level did not significantly affect the resonance curve fitting in the data analysis, it is sufficient to calibrate the network analyzer only at room temperature external to the cryostat.

The intrinsic Q factor of a resonator is obtained by fitting the measured resonance curve with ϕ -rotation model²⁶. To extract the dielectric loss from the overall loss, the quasiparticle loss, which is significant at liquid helium temperature, should be determined first. The Q factor of the resonators measured at relatively high temperature ($>5 \text{ K}$, or $0.6 T_c$) was used in quantifying the quasiparticle loss because model predictions safely indicate that quasiparticle loss is dominant at these temperatures. that quasiparticle loss is dominant at these tempera-

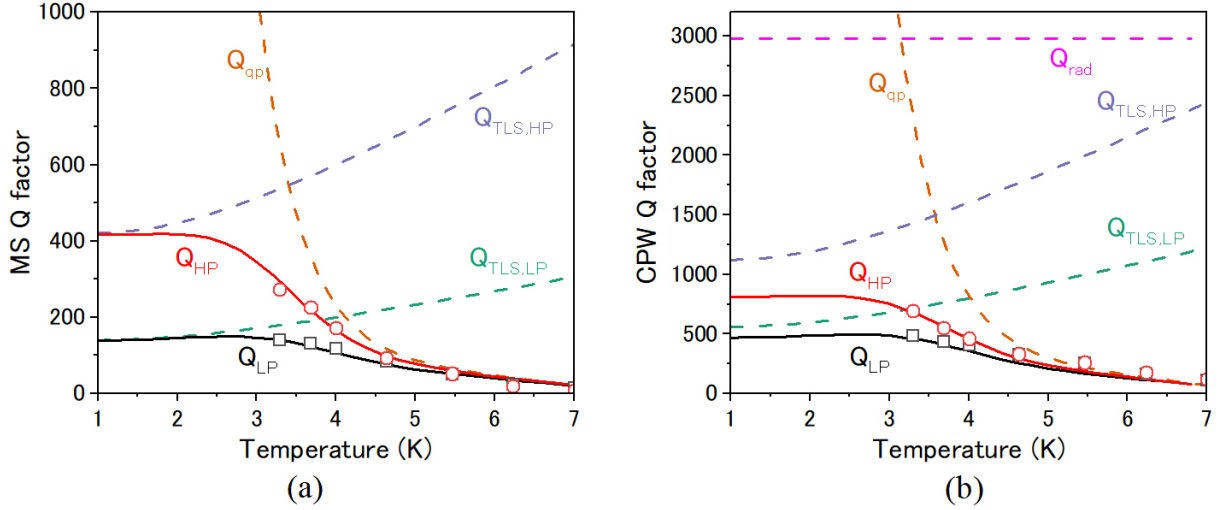


FIG. 3. (a) Measured (dots) and modeled (solid lines) intrinsic Q factor of an MS resonator and (b) a CPW resonator with respect to ambient temperature under high power (Q_{HP} at $3 \mu\text{W}$) and low power (Q_{LP}). The overall Q is decomposed into compositions of quasiparticle (Q_{qp}), TLS (Q_{TLS}) and radiation (Q_{rad}) losses, depicted in dashed lines.

tures. We applied a transmission line model to align the calculated loss with the measured one at this temperature range by tuning material parameters of niobium, as detailed in the appendix. Then, the quasi-particle loss at lower temperature was calculated by using this refined model and subtracted from the overall loss to obtain the dielectric loss. Additionally, because TLS loss is strongly dependent on frequency according to the factor $\tanh(\hbar\omega/k_B T)$, we also fabricated MS resonators resonating at approximately 5 GHz using the same fabrication process as for millimeter resonators. This approach provides an extended scope to identify the nature of the dielectric loss.

TLS losses are distinctive due to their unique power-dependence feature. At temperatures lower than 5 K, the power-dependences of the intrinsic Q factor of both MS and CPW resonators were clearly observed. An example of an MS resonator measured at 3.3 K is shown in the inset of Fig. 2. After removing the quasiparticle loss, the dielectric Q factors are plotted against signal power in Fig. 2. The data align well with the standard TLS model shown in Eq. 1, with an intrinsic TLS loss $\delta_{TLS}^0 \approx 6.7 \times 10^{-3}$ for SiO₂ deposited by using PECVD and a critical power $P_c \approx 0.3 \mu\text{W}$, corresponding to a field of $E_c \approx 0.5 \text{MV/m}$. In the fitting of TLS loss, we have assumed that the losses other than the quasiparticle loss and the TLS loss can be neglected. This assumption is justified for two reasons: First, any frequency-independent loss comparable to the two major losses can be ruled out, as the microwave version of the resonators at about 5 GHz show significantly lower loss by a factor of 20 at 4 K; and second, the only known frequency-dependent radiation loss is not relevant in MS.

The temperature dependence of the intrinsic Q factor of MS and CPW resonators was measured under both weak ($P \ll P_c$) and strong power (about $3 \mu\text{W}$). The measured temperature dependence closely matches the model, with δ_{TLS}^0 and P_c for TLS loss and σ_n for quasiparticle loss determined experimentally. Examples for an MS resonator and a CPW resonator

with PECVD-deposited SiO₂ are shown in Fig. 3. The breakdown of the intrinsic Q factor into the major compositions was performed using the previously discussed quasiparticle and TLS models, as well as a radiation loss model^{27,28} for the CPW resonator. The radiation loss of the CPW, with a configuration of slot/stripe/slot= $4 \mu\text{m}/2 \mu\text{m}/4 \mu\text{m}$ on silicon substrate, is predicted to be insignificant at this frequency band compared to other losses. One important observation is that the quasiparticle loss of niobium and the dielectric loss will become comparable and exchange their leading roles in the temperature range between 3 to 4 K. Even if the TLS noise can be reduced to some extent by improving fabrication techniques, the crossover still occurs in this temperature range because, there, the quasiparticle loss rapidly reduces with temperature.

The power dependence of the intrinsic Q factor of the CPW resonator is weaker than that of MS resonators, as shown by comparing Fig. 3(a) with (b). It is because the TLS loss is reduced by the filling factor. We applied buffered HF etch to the chips containing CPW resonators to remove the SiO₂ in the slots and partly under the strips. Although the remove of SiO₂ caused an upward frequency shift of the resonator by about 20%, some resonators remained still within the measurement frequency range, allowing us to confirm that the power dependence of the resonance curves became unobservable. For MS resonators, however, the resonance frequencies became too high and fell outside the measurable frequency range.

Resonators with sputtered SiO₂ layer fabricated using a magnetron RF plasma system were also measured. Measured results show $\delta_{TLS}^0 \approx 3 \times 10^{-3}$, which is factor of 2 smaller than those deposited with PECVD. These results align with those measured by others at similar frequency range: a tangential loss of 5.3×10^{-3} for sputtered SiO₂ at frequencies between 75-100 GHz and at 4.2 K were reported by Vayonakis et al.²², and losses ranging from $0.5 - 2 \times 10^{-3}$ at approximately 100 GHz and 30 mK were observed by Gao et

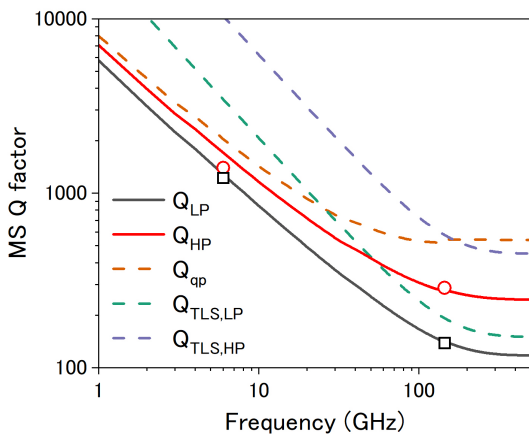


FIG. 4. Measured intrinsic Q factors (dots) of microwave and millimeter-wave MS resonators at 3.3 K under strong power (about $3 \mu\text{W}$) and low power ($P \ll P_c$). Solid lines represent the model-predicted Q factors as a function of frequency up to sub-millimeter range. Dashed lines depict the decomposed TLS noises (under high power and low power) and quasiparticle loss.

al.²⁹, with both measurements conducted using superconducting MS resonators. At microwave frequencies, more measurement data¹ show a wider range of δ_{TLS}^0 from 3×10^{-4} to 7×10^{-3} .

At 5 GHz, the TLS loss is predicted to be significantly smaller than that at 140 GHz, becoming less significant than the quasiparticle loss. This makes identification of TLS loss at 4 K difficult at microwave. In our measurement, the intrinsic Q factor of MS resonators with SiO_2 deposited with PECVD were found to be about 1.4×10^3 . After correcting for the quasiparticle loss, the weak-field dielectric loss is about 2.5×10^{-4} , corresponding to $\delta_{TLS}^0 \approx 7 \times 10^{-3}$, which is very close to the intrinsic TLS loss obtained at 2 mm wavelength. We observed a weak power dependence of the intrinsic Q factor. When the input power, corrected for the transmission loss, was increased to $3 \mu\text{W}$, which is the "high power" applied in mm measurement, the intrinsic Q factor increased by about 10% with respect to the weak-field value, as shown in Fig. 4. The increase is about 40% of that predicted by the model, which assumes that P_c is independent of frequency. This suggests that P_c at about 5 GHz is as large approximately twice the value at about 140 GHz.

Assuming that the density of states and saturation power of TLSs, which are expected to be smoothly dependent frequency, remain constant in a frequency range from about 140 GHz to the gap frequency of niobium, we can make meaningful predictions for the niobium MS loss at sub-millimeter range, as shown in Fig. 4. It is found that TLS loss and quasiparticle loss tend to level off as frequency increases toward the sub-millimeter range. Therefore, their relative values will not change significantly compared to those at 140 GHz. This is a favorable signal for the sub-millimeter applications at 4 K using MS lines. For superconducting CPWs, the radiation loss may become dominate at submillimeter waves^{30,31}.

In conclusion, we have measured the power-dependent intrinsic Q factor of both SiO_2 -loaded MS and CPW resonators

at 2 mm wavelength and found that they can be accurately modeled using the TLS model. At liquid helium temperatures, the TLS loss of amorphous SiO_2 may become a dominant factor in planar superconducting transmission lines, in particular MSs, operating at millimeter and sub-millimeter wavelengths. This study highlights the significance of TLS loss at 4 K, where a crossover between quasiparticle loss and TLS loss occurs, providing crucial insights for the design of superconducting devices operating in this temperature range.

ACKNOWLEDGMENTS

The work is partly supported by the Japan Society for the Promotion of Science (JSPS) KAKENHI under Grant Number 23K20871.

SUPPLEMENTARY MATERIAL

See the supplementary material for detailed information, including measurement setup, resonator design and fabrication, and correction for quasiparticle loss.

A. Measurement setup

The measurement setup, as shown in Fig. 5(a) employs an Agilent E8362C vector network analyzer (NA) and an N5260A millimeter head controller together with OML V06VNA2 millimeter wave VNA extenders. A D-band variable attenuator is used to vary the signal power. The millimeter wave monolithic integrated circuit (MMIC) containing resonators is mounted in an aluminum enclosure with build-in waveguides and standard waveguide interfaces. This unit, referred to as device-under-test (DUT), is thermally anchored to the 4-K cold stage and connected to the NA with thermal-insulating CuNi WR-6 waveguides on each side, with each having an attenuation of about 10 dB. The power measured at the output of the millimeter wave transducer is approximately $30 \mu\text{W}$ using an mm-wave powermeter Erikson PM4. The structure of the DUT is illustrated in Fig. 5(b) and 5(c). Two embedded waveguide H-bends are designed to have a passband wider than the silicon membrane-based waveguide-to-CPW transitions. The measured transmission performance of this module is detailed in a previous study²⁵.

B. Resonator design and fabrication

The ground plane and the conducting strips for MSs and CPWs were made from niobium thin films with thickness of about 200 nm. The conducting strip width of MSs and CPWs are $3 \mu\text{m}$ and $2 \mu\text{m}$ respectively. The configurations of CPWs for readout and resonators are $4 \mu\text{m}/2 \mu\text{m}/4 \mu\text{m}$ (slot/stripe/slot) for mm-wave resonators and $5 \mu\text{m}/10 \mu\text{m}/5 \mu\text{m}$ for the readout CPW at microwave frequencies. Microscopic images of the resonators are shown

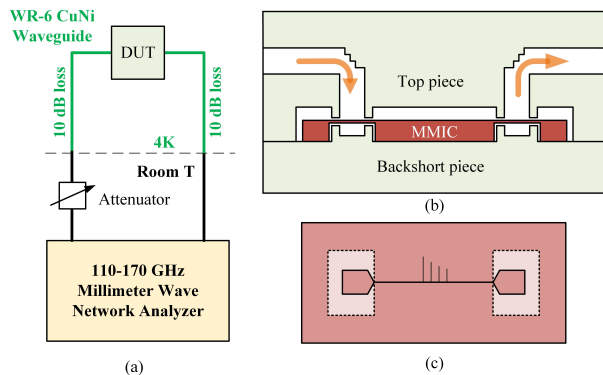


FIG. 5. Setup for millimeter wave resonator measurement. (a) Diagram of the measurement system. (b) Schematic structure of the enclosure of the MMIC containing resonators. (c) Schematic top-view of the MMIC.

in Fig. 6. The SiO_2 is 300 nm thick for mm-wave resonators and 200 nm thick for microwave resonators; this layer completely covers all the wafer above the ground patterns. The resonators couple signals from the readout line using parallel plate capacitors with the same SiO_2 layer as dielectric material. The bottom plate of each capacitor, a patch isolated from the ground plane, is connected to the center strip of the resonator through a conducting via hole cross the SiO_2 layer. The symmetry of the CPW is disrupted at the coupling T-junctions because resonators are asymmetrically coupled on one side. The broken symmetry may stimulate the CPW odd mode, leading to a reduction in intrinsic Q. To avoid the odd mode generation, bridges were used to connect the ground planes of the readout CPW around the T-junctions. The bridges were made on the ground plane to ease the fabrication, rather than using conventional air-bridges. They cause negligible reflection because the bridges are electrically very short.

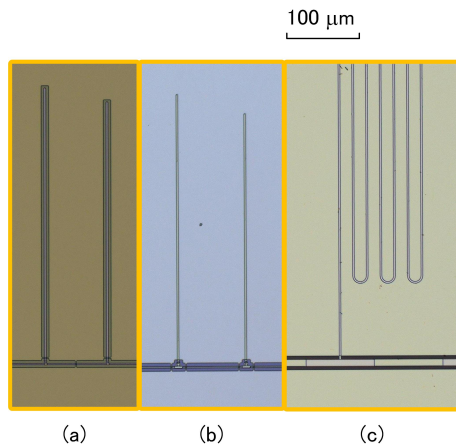


FIG. 6. Microscopic images of (a) millimeter wave CPW resonators, (b) millimeter wave MS resonators, and (c) a microwave MS resonators.

Niobium was deposited using DC magnetron sputtering at a substrate temperature 20°C . T_c was measured about 8.9 K .

The film exhibited compressive stress of about -0.65 GPa , and the resistivity at room temperature is about $18.6\ \mu\Omega\text{cm}$. The residual resistance ratio was measured to be 4.5, resulting in a residual resistivity approximately $4.2\ \mu\Omega\text{cm}$ at the temperature immediately above the superconducting transition. SiO_2 was deposited in a PECVD system, Samco PD-200STL, using tetraethyl orthosilicate (TEOS) as the precursor. The deposition was carried out in an oxygen-rich atmosphere with flow rate of TEOS and O_2 at 15 and 680 sccm respectively, and a pressure of 40 Pa. The reactor temperature was set to be 100°C , and the plasma power was 350 W. The resulting film exhibited a compressive stress of about -0.32 GPa . For some devices, RF magnetron sputter (UL-VAC MB951011) was used. The film was sputtered in an argon plus 10% oxygen atmosphere at 3.6 Pa and 400 W at room temperature. The film was nearly stress-free.

C. Correction for quasiparticle loss

To extract the dielectric loss from the overall loss of a resonator implied by intrinsic Q factor, it is necessary to correctly determine the quasiparticle loss. The quasiparticle loss of an MS was calculated by combining the Mattis-Bardeen theory³² and a conformal mapping technique^{33,34}, which takes into account the geometric configuration of the MS. Our first attempt to calculate the quasiparticle loss with using the measured niobium residue resistivity $4.2\ \mu\Omega\text{cm}$ was inconsistent with the measurement results. The calculated quasiparticle loss at $T > 5\text{ K}$, where quasiparticle loss is dominant, was about half as large as measured values. The analytical transmission line model is unlikely to have caused the discrepancy because numerical simulations using EM field simulator (HFSS³⁵) and complex surface impedances³⁶ resulted in very similar results to the analytical ones. We tried tuning the niobium parameters, including gap voltage (nominally 2.8 mV), T_c (8.9 K measured), conductivity, and electron density ($5.6 \times 10^{28}\text{ m}^{-3}$) to make the calculated results approach the measured ones and found that conductivity is the most sensitive and likely the responsible parameter. The inconsistency can be alleviated if the niobium residue resistivity is set to $12.5\ \mu\Omega\text{cm}$, about three times the value measured at DC. This implies that the niobium film has inhomogeneous quality with a degraded epilayer contributing most to RF loss, though this degradation cannot be reflected in the DC measurement. This phenomenon is also observed by Lodewijk etc.³⁷, and is supported by the fact that niobium film quality is strongly dependent on thickness, showing a gradually development of texture in the initial layer³⁸⁻⁴⁰. The effective residual resistivity was applied in the theoretical model to separate the quasiparticle loss and the dielectric loss in the data analysis.

It is worth noting that even though there is some uncertainty in the determination of quasiparticle loss, it does not significantly affect the extraction of dielectric loss at 4 K and lower temperatures. This is because the quasiparticle loss, calculated with either nominal or effective residual conductivity, becomes relatively unimportant compared to the dielectric loss, and does not qualitatively affect the conclusion. By us-

ing the effective residual resistivity, the consistency between the model and the measurement is achieved over a broad temperature range. The good match between the simulated and measured temperature dependence further justifies the use of the effective conductivity.

- ¹C. R. H. McRae, H. Wang, J. Gao, M. R. Vissers, T. Brecht, A. Dunsworth, D. P. Pappas, and J. Mutus, "Materials loss measurements using superconducting microwave resonators," *Review of Scientific Instruments* **91** (2020).
- ²C. A. Hamilton, C. J. Burroughs, and S. P. Benz, "Josephson voltage standard—a review," *IEEE transactions on applied superconductivity* **7**, 3756–3761 (1997).
- ³W. Chen, A. Rylyakov, V. Patel, J. Lukens, and K. Likharev, "Superconductor digital frequency divider operating up to 750 GHz," *Applied physics letters* **73**, 2817–2819 (1998).
- ⁴I. I. Soloviev, N. V. Klenov, S. V. Bakurskiy, M. Y. Kupriyanov, A. L. Gudkov, and A. S. Sidorenko, "Beyond moore's technologies: operation principles of a superconductor alternative," *Beilstein journal of nanotechnology* **8**, 2689–2710 (2017).
- ⁵H. Maezawa, "Application of superconducting hot-electron bolometer mixers for terahertz-band astronomy," *IEICE Transactions on Electronics* **98**, 196–206 (2015).
- ⁶A. Shurakov, Y. Lobanov, and G. Goltsman, "Superconducting hot-electron bolometer: from the discovery of hot-electron phenomena to practical applications," *Superconductor Science and Technology* **29**, 023001 (2015).
- ⁷F. Mena, J. Kooi, A. Baryshev, C. Lodewijk, T. Zijlstra, R. Hesper, G. Gerlofsma, T. Klapwijk, and W. Wild, "Design and performance of a 600–720 GHz sideband-separating receiver using AlO_x and AlN SIS junctions," *IEEE Transactions on Microwave Theory and Techniques* **59**, 166–177 (2010).
- ⁸S. Mahieu, D. Maier, B. Lazareff, A. Navarrini, G. Celestin, J. Chalaïn, D. Geoffroy, F. Laslaz, and G. Perrin, "The ALMA band-7 cartridge," *IEEE Transactions on Terahertz Science and Technology* **2**, 29–39 (2011).
- ⁹A. R. Kerr, S.-K. Pan, S. M. Claude, P. Dindo, A. W. Lichtenberger, J. E. Effland, and E. F. Lauria, "Development of the ALMA band-3 and band-6 sideband-separating SIS mixers," *IEEE Transactions on Terahertz Science and Technology* **4**, 201–212 (2014).
- ¹⁰V. Belitsky, M. Bylund, V. Desmaris, A. Ermakov, S.-E. Ferm, M. Fredrixon, S. Krause, I. Lapkin, D. Meledin, A. Pavolotsky, *et al.*, "ALMA Band 5 receiver cartridge-design, performance, and commissioning," *Astronomy & Astrophysics* **611**, A98 (2018).
- ¹¹Y. Uzawa, M. Kroug, T. Kojima, M. Takeda, K. Makise, S. Ezaki, W. Shan, A. Miyachi, Y. Fujii, and H. Terai, "Development of superconducting devices supporting radio astronomy," *IEICE Transactions on Electronics* **104**, 411–421 (2021).
- ¹²J. Hubmayr, J. Austermann, J. Beall, D. Becker, H.-M. Cho, R. Datta, S. Duff, E. Grace, N. Halverson, S. Henderson, *et al.*, "Feedhorn-coupled transition-edge superconducting bolometer arrays for cosmic microwave background polarimetry," in *International Symposium on Space Terahertz Technology*, GSFC-E-DAA-TN32074 (2015).
- ¹³J. Hubmayr, J. E. Austermann, J. A. Beall, D. T. Becker, S. J. Benton, A. S. Bergman, J. R. Bond, S. Bryan, S. M. Duff, A. J. Duivenvoorden, *et al.*, "Design of 280 GHz feedhorn-coupled TES arrays for the balloonborne polarimeter SPIDER," in *Millimeter, Submillimeter, and Far-Infrared Detectors and Instrumentation for Astronomy VIII*, Vol. 9914 (SPIE, 2016) pp. 185–198.
- ¹⁴A. Kerr, S. Pan, A. Lichtenberger, and H. Huang, "A tunerless SIS mixer for 200–280 GHz with low output capacitance and inductance," (1998).
- ¹⁵V. Koshelets and S. Shitov, "Integrated superconducting receivers," *Superconductor Science and Technology* **13**, R53 (2000).
- ¹⁶I. V. Vernik, D. E. Kirichenko, S. Sarwana, and D. K. Brock, "Integrated millimeter/submillimeter superconducting digital spectrometer," *IEEE transactions on applied superconductivity* **15**, 419–422 (2005).
- ¹⁷W. Shan, S. Ezaki, H. Kang, A. Gonzalez, T. Kojima, and Y. Uzawa, "A compact superconducting heterodyne focal plane array implemented with HPI (hybrid planar integration) scheme," *IEEE Transactions on Terahertz Science and Technology* **10**, 677–689 (2020).
- ¹⁸J. Wenninger, F. Boussaha, C. Chaumont, B.-K. Tan, and G. Yassin, "Design of a 240 GHz on-chip dual-polarization receiver for SIS mixer arrays," *Superconductor Science and Technology* **36**, 055012 (2023).
- ¹⁹C. Groppi, A. Baryshev, U. Graf, M. Wiedner, P. Klaassen, and T. Mroczkowski, "First generation heterodyne instrumentation concepts for the atacama large aperture submillimeter telescope," arXiv preprint arXiv:1907.03479 (2019).
- ²⁰P. W. Anderson, B. I. Halperin, and C. M. Varma, "Anomalous low-temperature thermal properties of glasses and spin glasses," *Philosophical Magazine* **25**, 1–9 (1972).
- ²¹W. A. Phillips, "Two-level states in glasses," *Reports on Progress in Physics* **50**, 1657 (1987).
- ²²A. Vayonakis, C. Luo, H. Leduc, R. Schoelkopf, and J. Zmuidzinas, "The millimeter-wave properties of superconducting microstrip lines," in *AIP Conference Proceedings*, Vol. 605 (American Institute of Physics, 2002) pp. 539–542.
- ²³W. Shan and S. Ezaki, "Investigating millimeter-wave thin-film superconducting resonators: A study using tunnel junction detectors," arXiv preprint arXiv:2403.12342 (2024).
- ²⁴M. Schubert, S. Anders, E. Haertel, G. Wende, R. Hähle, L. Fritsch, M. Starkloff, U. Springborn, F. Müller, J. Kohlmann, *et al.*, "Microwave properties of microstrip line circuits used for Josephson voltage standard arrays at 70 GHz," *Superconductor Science and Technology* **24**, 085006 (2011).
- ²⁵A. Masukura, W. Shan, S. Ezaki, T. Kojima, T. Nakajima, and A. Mizuno, "Silicon membrane-based waveguide-to-superconducting cpw transitions at 2 mm band," *IEEE Transactions on Applied Superconductivity* (2023).
- ²⁶J. Gao, *The physics of superconducting microwave resonators* (California Institute of Technology, 2008).
- ²⁷D. P. Kasilingam and D. B. Rutledge, "Surface-wave losses of coplanar transmission lines," in *1983 IEEE MTT-S International Microwave Symposium Digest* (IEEE, 1983) pp. 113–116.
- ²⁸D. B. Rutledge, D. P. Neikirk, and D. P. Kasilingam, "Integrated circuit antennas," *Infrared and millimeter waves* **10**, 1–90 (1983).
- ²⁹J. Gao, A. Vayonakis, O. Noroozian, J. Zmuidzinas, P. K. Day, and H. G. Leduc, "Measurement of loss in superconducting microstrip at millimeter-wave frequencies," in *AIP Conference Proceedings*, Vol. 1185 (American Institute of Physics, 2009) pp. 164–167.
- ³⁰D. Grischkowsky, I. Duling III, J. Chen, and C.-C. Chi, "Electromagnetic shock waves from transmission lines," *Physical review letters* **59**, 1663 (1987).
- ³¹S. Hähnle, N. v. Marrewijk, A. Endo, K. Karatsu, D. Thoen, V. Murugesan, and J. Baselmans, "Suppression of radiation loss in high kinetic inductance superconducting co-planar waveguides," *Applied Physics Letters* **116**, 182601 (2020).
- ³²D. C. Mattis and J. Bardeen, "Theory of the anomalous skin effect in normal and superconducting metals," *Physical Review* **111**, 412 (1958).
- ³³W. Chang, "Analytical ic metal-line capacitance formulas (short papers)," *IEEE Transactions on Microwave Theory and Techniques* **24**, 608–611 (1976).
- ³⁴S. Gevorgian, L. P. Linner, and E. L. Kollberg, "CAD models for shielded multilayered CPW," *IEEE transactions on microwave theory and techniques* **43**, 772–779 (1995).
- ³⁵ANSYS, "HFSS:3D electromagnetic field simulator for RF and wireless design," (2024).
- ³⁶A. R. Kerr, "Surface impedance of superconductors and normal conductors in EM simulators," MMA Memo No. 245 (1999).
- ³⁷C. Lodewijk, O. Noroozian, D. Loudkov, T. Zijlstra, A. Baryshev, F. Mena, and T. Klapwijk, "Optimizing superconducting matching circuits for Nb SIS mixers operating around the gap frequency," *IEEE transactions on applied superconductivity* **17**, 375–378 (2007).
- ³⁸M. Minhaj, S. Meepagala, J. Chen, and L. Wenger, "Thickness dependence on the superconducting properties of thin Nb films," *Physical Review B* **49**, 15235 (1994).
- ³⁹V. Lacquaniti, S. Maggi, E. Monticone, and R. Steni, "Thickness dependence of electrical and structural properties of Nb thin films," *physica status solidi (a)* **151**, 335–344 (1995).
- ⁴⁰A. Chandrasekaran, R. W. van de Kruijs, J. M. Sturm, and F. Bijkerk, "Nb texture evolution and interdiffusion in Nb/Si-layered systems," *ACS Applied Materials & Interfaces* **13**, 31260–31270 (2021).